Heterogeneous Catalysis

DOI: 10.1002/anie.201200699

Hydrogen-Evolution Catalysts Based on Non-Noble Metal Nickel–Molybdenum Nitride Nanosheets**

Wei-Fu Chen, Kotaro Sasaki, Chao Ma, Anatoly I. Frenkel, Nebojsa Marinkovic, James T. Muckerman, Yimei Zhu, and Radoslav R. Adzic*

Hydrogen production through splitting of water has attracted great scientific interest because of its relevance to renewable energy storage and its potential for providing energy without the emission of carbon dioxide.[1] Electrocatalytic systems for H_2 generation typically incorporate noble metals such as Pt in the catalysts because of their low overpotential and fast kinetics for driving the hydrogen evolution reaction (HER). However, the high costs and limited world-wide supply of these noble metals make their application in viable commercial processes unattractive. Several non-noble metal materials, such as transition-metal chalcogenides,[2] carbides,[3] and complexes[4] as well as metal alloys[5] have been widely investigated recently, and characterized as catalysts and supports for application in the evolution of hydrogen.

Nitrides of early transition-metals have been shown to have excellent catalytic activities in a variety of reactions.[6] One of the primary interests in the applications of nitrides in these reactions was to use them in conjunction with low-cost alternative metals to replace group VIII noble metals. For example, the function of molybdenum nitride as a catalyst for hydrocarbon hydrogenolysis resembles that of platinum.[7] The catalytic and electronic properties of transition-metal nitrides are governed by their bulk and surface structure and stoichiometry. While there is some information concerning the effect of the bulk composition on the catalytic properties of this material, there is currently little known about the effects of the surface nanostructure.

Nickel and nickel–molybdenum are known electrocatalysts for hydrogen production in alkaline electrolytes, and in the bulk form they exhibited exchange current densities between 10^{-6} and 10^{-4} A cm^{-2}, compared to 10^{-3} A cm^{-2} for Pt.[8] Jakšić et al.[9] postulated a hypo-hyper-d-electronic interactive effect between Ni and Mo that yields the synergism for the HER. Owing to their poor corrosion stability, few studies in acidic media have been reported. With the objective of exploiting the decrease in the overpotential by carrying out the HER in acidic media, we have developed a low-cost, stable, and active molybdenum-nitride-based electrocatalyst for the HER.

Guided by the "volcano plot"[10] in which the activity for the evolution of hydrogen as a function of the M–H bond strength exhibits an ascending branch followed by a descending branch, peaking at Pt, we designed a material on the molecular scale combining nickel, which binds H weakly, with molybdenum, which binds H strongly. Here we report the first synthesis of NiMo nitride nanosheets on a carbon support ($NiMoN_x$/C), and demonstrate the high HER electrocatalytic activity of the resulting $NiMoN_x$/C catalyst with low overpotential and small Tafel slope.

The $NiMoN_x$/C catalyst was synthesized by reduction of a carbon-supported ammonium molybdate $[(NH_4)_6Mo_7O_{24}\cdot 4H_2O]$ and nickel nitrate $(Ni(NO_3)_2\cdot 4H_2O)$ mixture in a tubular oven in H_2 at 400 °C, and subsequent reaction with NH_3 at 700 °C. During this process, the $(NH_4)_6Mo_7O_{24}$ and $Ni(NO_3)_2$ precursors were reduced to NiMo metal particles by H_2, and then they were mildly transformed to $NiMoN_x$ nanosheets by reaction with ammonia. The atomic ratio of Ni/Mo was 1/4.7 determined by energy dispersive X-ray spectroscopy (EDX) on the $NiMoN_x$/C sample. The transmission electron microscopy (TEM) images, as shown in Figure 1 a, display NiMo particles that are mainly spherical. The high-resolution TEM image, as shown in the inset of Figure 1 a, corroborated the presence of an amorphous 3 to 5 nm Ni/Mo oxide layer (see Figure S4 in the Supporting Information for resolved image), whereas $NiMoN_x$ is characterized by thin, flat, and flaky stacks composed of nanosheets with high radial-axial ratios (Figure 1 b and Figure S5 in the Supporting Information for a magnified image). Figure 1 c shows that some of the nanosheets lay flat on the graphite carbon (as indicated by the black arrows), and some have folded edges that show different layers of $NiMoN_x$ sheets (white arrows). The thickness of the sheets ranged from 4 to 15 nm. The average stacking number of sheets measured from Figure 1 b is about

[*] Dr. W.-F. Chen, Dr. K. Sasaki, Dr. J. T. Muckerman, Dr. R. R. Adzic
Chemistry Department, Brookhaven National Laboratory
Upton, NY 11973 (USA)
E-mail: ksasaki@bnl.gov
Dr. C. Ma, Dr. Y. Zhu
Condensed Matter Physics & Materials, Science Department
Brookhaven National Laboratory, Upton, NY 11973 (USA)
Dr. A. I. Frenkel
Physics Department, Yeshiva University
245 Lexington, Avenue, New York, NY 10016 (USA)
Dr. N. Marinkovic
Department of Chemical Engineering, University of Delaware
Newark, DE 19716 (USA)

[**] This work was carried out at Brookhaven National Laboratory (BNL) with the U.S. Department of Energy (DOE) under contract number DE-AC02-98CH10886 and supported by BNL Laboratory Directed Research and Development (LDRD) (project number 10-015). A.I.F. acknowledges support by DOE BES (grant number DE-FG02-03ER15476). Beamlines X19A and X18B at the NSLS are supported in part by the Synchrotron Catalysis Consortium, U.S. Department of Energy (grant number DE-FG02-05ER15688).

Supporting information for this article is available on the WWW under http://dx.doi.org/10.1002/anie.201200699.

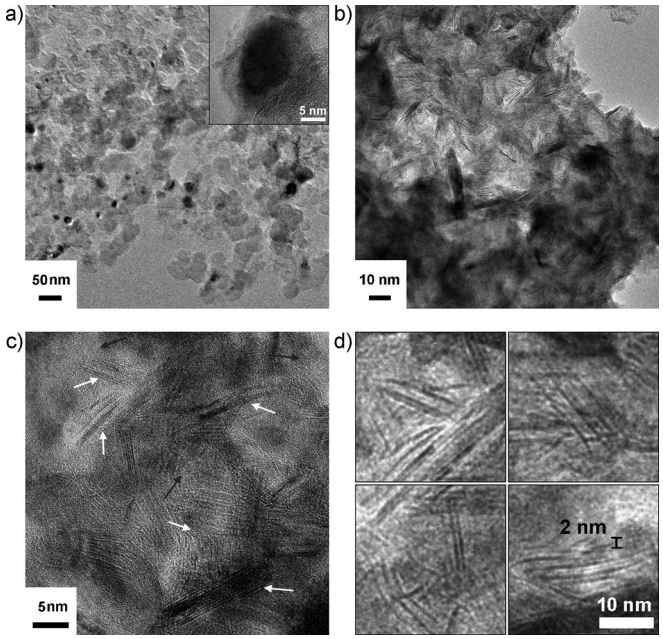

Figure 1. TEM images of a) carbon-supported NiMo nanoparticles (NiMo/C) reduced in H_2 at 500 °C and b) $NiMoN_x$ nanosheets prepared by treating the NiMo/C in NH_3 flow at 700 °C. c) High-resolution TEM images of $NiMoN_x$. d) Magnified images showing exfoliated $NiMoN_x$ nanosheets.

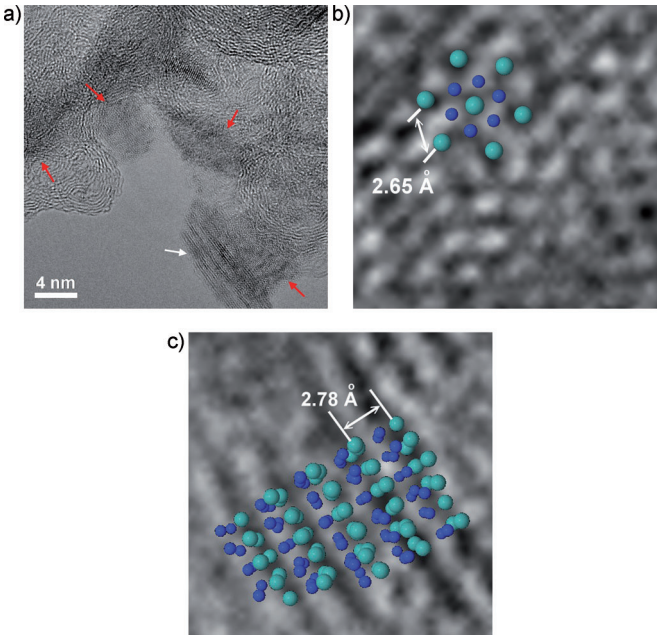

Figure 2. a) TEM image of the stacked MoN nanosheets on carbon supports. The red and white arrows mark the nanosheets that lay flat and stand vertically, respectively. b) A HRTEM image with the crystal structure overlaid looking down along the <002> zone axis, and c) a HRTEM image showing the standing {002} lattice planes (cyan balls: Mo and small blue balls: N).

six. A major part of the nanosheets was exfoliated and present in the form of single sheets. The HRTEM images in Figure 1d show the morphology of these single sheets. The gap between two single sheets was found to be up to 2 nm.

Carbon-supported molybdenum nitride nanosheets (MoN/C, Figure 2a) were also prepared by the same procedure as $NiMoN_x$/C. HRTEM revealed hexagonal lattices of the δ-MoN nanosheets in the $\langle 002 \rangle$ (Figure 2b) and $\langle 200 \rangle$ (Figure 2c) directions.

A structural transformation from NiMo particles to $NiMoN_x$ sheets was observed by XRD; the patterns of the mixture of the Ni and Mo precursors, H_2-reduced NiMo/C and $NiMoN_x$/C are compared in Figure 3a. The Ni–Mo bimetallic nitrides were found to contain a majority of γ-Mo_2N (JCPDS PDF 25-1366) and Ni_2Mo_3N phases[11] (Figure S6 in the Supporting Information). The lengths (D_{hkl}) of the $NiMoN_x$ sheets along the stacking and basal directions were calculated using the Debye–Scherer equation (see the Supporting Information for details). The calculated D_{111} and D_{200} are 5.9 and 12.8 nm, respectively. The stacking number of the sheets can be calculated using $\tilde{n} = D_{hkl}/d_{hkl}$. The average stacking number for the (200) plane is 6.1 layers, which agrees well with the above TEM result.

We applied X-ray absorption near-edge structure (XANES) and extended X-ray absorption fine structure (EXAFS) spectroscopies to probe the charge states and the local structure in the $NiMoN_x$ and MoN nanosheets. The Ni K-edge XANES spectrum from NiMo particles in Figure 3b shows a strong white line signal at 8350 eV which indicates that the NiMo alloy particles formed Ni oxide particles, in contrast to Ni atoms in $NiMoN_x$ which are found in the metallic state. For the Mo K-edge (Figure 3c), the presence of the pre-edge feature of the NiMo alloy at 20004 eV reflects the existence of holes in the d-band, which can be ascribed to an increased oxidation state of the Mo atoms. In contrast, the white line at the Mo K-edge for $NiMoN_x$ exhibits a significant change compared to the NiMo alloy. Chen[12] showed that the density of states of the unfilled d-band of Mo can be modified as a metal–nitrogen bond is formed. Thus, the low Ni and Mo valences in $NiMoN_x$ can be reasonably ascribed to the lower deficiency in the d-band occupation of Mo which causes the $NiMoN_x$ to possess an electron-donating ability, and to enhance its catalytic activity for reactions involving the donation of d electrons, that is, in the HER.

The EXAFS spectra at the Ni K-edge of the $NiMoN_x$ are shown in Figure 3d. The peak at 2.18 Å originates from three almost superimposed bands at 1.5 Å for the Ni–N bond, at 2.2 Å for the Ni–Ni bond, and at 2.5 Å for the Ni–Mo bond (all distances are not corrected for the photoelectron phase shift). This peak is shifted to a higher r and broadened compared with that from a Ni foil (Figure S7 in the Supporting Information, in which the EXAFS spectra at the Mo K-edge are also shown). The differences between the nanosheets and their reference materials are apparent in the spectra, indicating that the atomic structures surrounding Ni and Mo in the $NiMoN_x$ nanosheets are significantly different from those in the bulk material. The data at the Ni K-edge from $NiMoN_x$ were fitted with models constructed from the Ni_2Mo_3N β-manganese structure as found in the literature[13] (see Table S1 in the Supporting Information). Good agreement was obtained between the fit and the experimental spectra (Figure 3d). The Ni–Ni bond distance ($R_{Ni\text{-}Ni}$) in

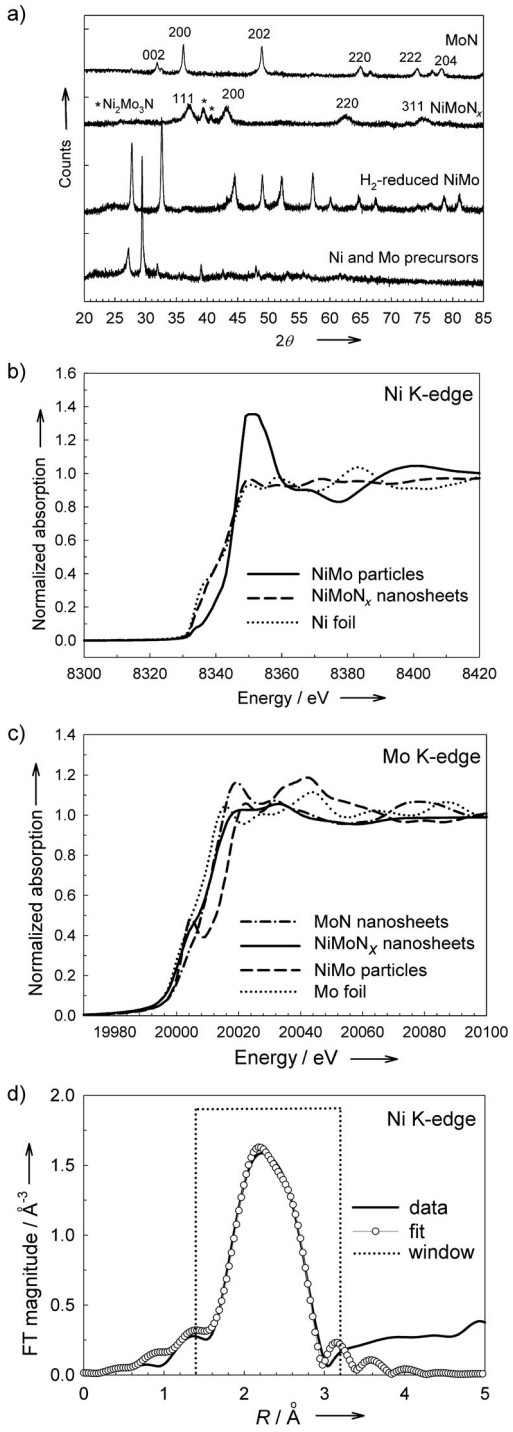

Figure 3. a) XRD patterns of carbon-supported MoN, $NiMoN_x$, H_2-reduced NiMo, and NiMo precursors. XANES spectra of b) Ni K- and c) Mo K-edges from NiMo nanoparticles and $NiMoN_x$ nanosheets as well as Ni and Mo foils. d) Fourier transformed magnitudes of the k^2-weighted Ni K-edge EXAFS data and first-shell fit for $NiMoN_x$ (k = the photoelectron wavenumber).

$NiMoN_x$ of (2.502 ± 0.019) Å is slightly longer than those in bulk Ni material (2.490 Å) and in Ni_2Mo_3N (2.468 Å). In contrast, the Ni–Mo bond distance ($R_{Ni\text{-}Mo}$) in $NiMoN_x$ of (2.748 ± 0.026) Å is found to be shorter than that in the bulk NiMo alloy of 2.800 Å. The coordination numbers obtained from the fitting analysis show the notably higher value of 7.3 ± 1.5 for Ni–Ni bonds compared to that in bulk Ni_2Mo_3N material ($N_{Ni\text{-}Ni,bulk} = 3.0$), whereas a lower number for Ni–Mo bonds was found ($N_{Ni\text{-}Mo} = 4.7 \pm 1.5$ vs. 9.0 for the bulk material). This finding indicates that more Ni–Ni bonds are present in the Ni_2Mo_3N phase of the $NiMoN_x$ nanosheets.

A theoretical study on a solute–host system predicted the segregation of nickel to the surface of the NiMo alloy.[14] Recently Eijsbouts et al.[15] reported that Ni segregated from commercial $NiMo/Al_2O_3$ catalsyts during ultradeep hydrodesulfurization (HDS) of diesel fuel. In the present $NiMoN_x$ system, the high $N_{Ni\text{-}Ni}$ and low $N_{Ni\text{-}Mo}$ demonstrated that Ni segregated to the surface of $NiMoN_x$ and formed a Ni-rich domain. This result corresponds well to the previous EXAFS studies on the NiMo system. Bouwens et al.[16] described the decoration of MoS_2 edge sites with Ni in the NiMoS system as the result of segregation. Hamabe et al.[17] found that the Ni–Ni coordination number obtained from the spent NiMoS HDS catalyst was approximately three times greater than that of the fresh catalyst because of segregation, and they observed destacked MoS_2-like slabs. Therefore, the particle-to-sheet transformation observed in $NiMoN_x$ is highly related to the segregation of the Ni phase during the nitriding process.

We investigated the HER activities of $NiMoN_x$/C and MoN/C in 0.1 M $HClO_4$ solution using a typical three-electrode setup. As a reference point, we also performed measurements using a commercial Pt catalyst (E-TEK 20 wt% Pt/XC-72) exhibiting a high activity for the HER (with a near-zero overpotential).

In Figure 4a, the polarization curve from MoN/C showed a small onset potential of −157 mV versus a reversible hydrogen electrode (RHE) for the HER (determined from the semi-log plot as shown in Figure S2 in the Supporting Information), beyond which the cathodic current rose rapidly under more negative potentials. It was interesting to observe that the $NiMoN_x$/C catalyst showed an even more positive potential of −78 mV than MoN/C. In sharp contrast, the NiMo/C catalysts exhibited a further negative and indistinct potential for the HER and a small current density. The overpotential for the HER on the NiMo alloy does not agree with that reported in the literature (−72 to −93 mV vs. a normal hydrogen electrode, NHE).[18] The high overpotential of NiMo nanopaticles can partially be ascribed to the surface oxide layer formed upon exposure to air. (Details of the other factors as well as the effect of the oxide layers on the current are described in Figure S9 in the Supporting Information.) Linear voltammetry in 0.1 M $HClO_4$ solution demonstrated that the $NiMoN_x$/C catalyst is fairly corrosion-resistant in the electrolyte (Figure S8 in the Supporting Information); it showed a low current density up to a potential of +0.84 V versus RHE, indicating that the presence of nitrogen significantly stabilized $NiMoN_x$ nanosheets in an acidic medium. NiMo nanoparticles also showed a relatively low current density up to +0.6 V versus RHE; but this is presumably due to passivation by oxide layers, and eventually NiMo/C undergoes dissolution at higher potentials. The oxide formation on NiMo nanoparticles is also observed by XANES analysis. Although the presence of oxide layers imparts the

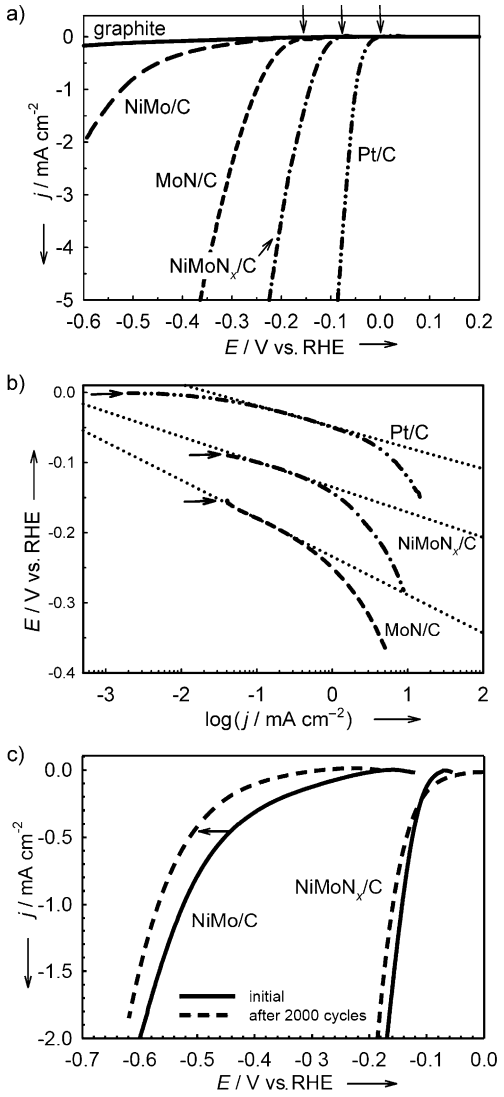

Figure 4. a) The polarization curves and b) corresponding Tafel plots of MoN, NiMoN$_x$, Pt/C catalysts, and graphite (XC-72) in 0.1 M $HClO_4$ solution (scan rate 2 mV s^{-1}). c) The polarization curves of NiMoN$_x$/C and H_2-reduced NiMo/C before and after potential sweeps (−0.3 + 0.9 V) for 2000 cycles in 0.1 M $HClO_4$ solution.

passivation in acidic solutions, it may deteriorate the catalytic activity, resulting in a high overpotential.

The Tafel curves recorded on NiMoN$_x$/C, MoN/C, and Pt/C (Figure 4b) exhibited classical Tafel behavior, clearly indicating that the HER can be described using the Tafel equation. The curves in the low current density region, as presented in Figure 4b, showed Tafel slopes of 30.1, 35.9, and 54.5 mV dec^{-1} for Pt, NiMoN$_x$/C, and MoN nanosheets, respectively. The Tafel curve of MoN clearly demonstrated that the HER occurs through a Volmer–Heyrovský mechanism, that is, the slow step is the electrochemical desorption of H_{ads} and H_3O^+ to form hydrogen. The HER onset potential and Tafel slope of bulk Mo metal are 0.23 V and 74 mV dec^{-1} (Figure S10 in the Supporting Information). The comparatively lower onset potential and the smaller Tafel slope of MoN than those of bulk Mo demonstrate that the presence of nitrogen in the Mo lattice favors proton adsorption kinetics. This can be attributed to the reduced ability of nitrides to donate d electrons as mentioned in the XANES section. The onset potentials, Tafel slopes, and exchange current densities are listed in Table 1 (the exchange current densities were determined as shown in Figure S3 in the Supporting Information).

Table 1: Onset potential, Tafel slope, and exchange current density (j_0) of different catalysts.

Catalyst	Onset potential [mV][a]	Tafel slope [mV dec^{-1}]	Exchange current density [mA cm^{-2}][b]
MoN/C	−157	54.5	0.036
NiMoN$_x$/C	−78	35.9	0.24
Pt/C	0	30.1	0.78

[a] The potential at which the hydrogen evolution occurred measured versus RHE. [b] Determined from Figure S3 in the Supporting Information.

For NiMoN$_x$, the low Tafel slope of 35.9 mV dec^{-1} suggests that the recombination of two H_{ads} is accelerated by the elimination of a part of the excess energy, liberated in the union of the two hydrogen atoms, by the NiMoN$_x$ surface. The HER mechanism appears to change as Ni is incorporated. Here hydrogen evolution occurs through a Tafel-like mechanism. As aforementioned in the EXAFS results, Ni segregates to the surface or edges of the Ni_2Mo_3N phase. The Ni–Ni distance was found to increase, but the Ni–Mo distance decreased upon nitride formation. The increase in the Ni–Ni distance causes the contraction of the Ni d-band, which would give a higher density of states near the Fermi level. On the other hand, the decrease in the Ni–Mo bond length downshifts the d-band center of the Mo atoms neighboring Ni relative to the Fermi level. The downshift of the d-band center has been correlated with a decrease in the hydrogen binding energy[19] which leads to a relatively moderate Mo–H binding strength, and in turn supports the recombination of two H_{ads} atoms.

Recently, Navarro-Flores et al.[5a] have proposed an electrocatalytic synergetic effect for enhanced hydrogen evolution kinetics on NiMo, NiW, and NiFe bimetallic alloys. Considering the exchange current density (j_0) of the NiMo alloy (20.5 μA cm^{-2}) presented by Navarro-Flores, the present NiMoN$_x$ catalyst exhibited a comparatively high j_0 of 0.24 mA cm^{-2} (j_0 was determined as described in Figure S3 in the Supporting Information). We attribute this high j_0 to the unique exfoliated sheet nanostructure that affords plenty of highly accessible reactive sites, and to the enhanced reaction kinetics because of the d-band modification as discussed above.

To assess the long-term durability of the NiMoN$_x$ catalyst, potential sweeps were conducted from −0.3 to +0.9 V for 2000 cycles. After cycling, the catalyst retained a polarization curve similar to that before testing (Figure 4c), indicating that the NiMoN$_x$ catalysts maintained its unique nanosheet structure over a long time in an acidic environment. The same experiment on the NiMo particles showed degradation

of the activity. These results afforded evidence for the stabilizing effect of nitrides on the NiMo bimetallic structure.

In conclusion, a heterogeneous electrocatalytic hydrogen-evolving system has been created from earth-abundant and inexpensive components. With highly exposed reactive sites and a synergism among its components, the $NiMoN_x$/C catalyst exhibited an excellent activity for the HER with a small overpotential of 78 mV, a high exchange current density, and a Tafel slope as small as 35 mV dec^{-1}. This is the smallest Tafel slope reported to date for a non-platinum catalyst, suggesting Tafel-like recombination as the rate-limiting step in the catalyzed HER. In acidic media, the $NiMoN_x$ nanosheets can be used without noticeable corrosion. Our XANES results provided an approach to understanding the electronic properties and the stabilizing effect of nitrogen on the metallic states of Ni and Mo. Further work is needed to characterize the local distribution of surface Ni and to optimize the ratio of components to improve the performance of this promising type of catalyst for the HER.

Received: January 25, 2012
Published online: May 8, 2012

Keywords: electrochemistry · evolution of hydrogen · heterogeneous catalysis · metal nitrides · nanosheets

[1] N. S. Lewis, D. G. Nocera, *Proc. Natl. Acad. Sci. USA* **2006**, *103*, 15729 – 15735.
[2] T. F. Jaramillo, K. P. Jørgensen, J. Bonde, J. H. Nielsen, S. Horch, I. Chorkendorff, *Science* **2007**, *317*, 100 – 102.
[3] D. V. Esposito, S. T. Hunt, A. L. Stottlemyer, K. D. Dobson, B. E. McCandless, R. W. Birkmire, J. G. Chen, *Angew. Chem.* **2010**, *122*, 10055 – 10058; *Angew. Chem. Int. Ed.* **2010**, *49*, 9859 – 9862.
[4] a) P. D. Tran, A. L. Goff, J. Heidkamp, B. Jousselme, N. Guillet, S. Palacin, H. Dau, M. Fontecave, V. Artero, *Angew. Chem.* **2011**, *123*, 1407 – 1410; *Angew. Chem. Int. Ed.* **2011**, *50*, 1371 – 1374; b) M. L. Helm, M. P. Stewart, M. Bullock, M. R. DuBois, D. L. DuBois, *Science* **2011**, *333*, 863 – 866.
[5] a) E. Navarro-Flores, Z. Chong, S. Omanovic, *J. Mol. Catal. A: Chem* **2005**, *226*, 179 – 197; b) J. R. McKone, E. L. Warren, M. J. Bierman, S. W. Boettcher, B. S. Brunschwig, N. S. Lewis, H. B. Gray, *Energy Environ. Sci.* **2011**, *4*, 3573 – 3583.
[6] a) Z. Wu, Z. Hao, P. Ying, C. Li, Q. Xin, *J. Phys. Chem. B* **2000**, *104*, 12275 – 12281; b) J. C. Schlatter, S. T. Oyama, J. E. Metcalfe III, J. M. Lambert, Jr., *Ind. Eng. Chem. Res.* **1988**, *27*, 1648 – 1653; c) D. Mckay, J. S. J. Hargreaves, J. L. Rico, J. L. Rivera, X.-L. Sun, *J. Solid State Chem.* **2008**, *181*, 325 – 333; d) S. T. Oyama, *Catal. Today* **1992**, *15*, 179 – 200; e) C. M. Cardona, B. Elliott, L. Echegoyen, *J. Am. Chem. Soc.* **2006**, *128*, 6480 – 6485.
[7] J.-G. Choi, J. R. Brenner, C. W. Colling, B. G. Demczyk, J. L. Dunning, L. T. Thompson, *Catal. Today* **1992**, *15*, 201 – 222.
[8] J. Y. Huot, M. L. Trudeau, R. Schulz, *J. Electrochem. Soc.* **1991**, *138*, 1316 – 1321.
[9] a) J. M. Jakšić, N. V. Krstajić, B. N. Grgur, M. M. Jakšić, *Int. J. Hydrogen Energy* **1998**, *23*, 667 – 681; b) M. M. Jakšić, *Int. J. Hydrogen Energy* **2001**, *26*, 559 – 578.
[10] M. M. Jakšić, *Int. J. Hydrogen Energy* **2001**, *26*, 559 – 578.
[11] a) W. Yuhong, L. Wei, Z. Minghui, G. Naijia, T. Keyi, *Appl. Catal. A* **2001**, *215*, 39 – 45; b) A. El-Himri, F. Sapiña, R. Ibañez, A. Beltrán, *J. Mater. Chem.* **2001**, *11*, 2311 – 2314.
[12] J. G. Chen, *Chem. Rev.* **1996**, *96*, 1477 – 1498.
[13] K. S. Weil, P. N. Kumta, J. Grins, *J. Solid State Chem.* **1999**, *146*, 22 – 35.
[14] A. V. Ruban, H. L. Skriver, J. K. Nørskov, *Phys. Rev. B* **1999**, *59*, 15990 – 16000.
[15] S. Eijsbouts, L. C. A. van den Oetelaar, R. R. van Puijenbroek, *J. Catal.* **2005**, *229*, 352 – 364.
[16] S. M. A. M. Bouwens, D. C. Koningsberger, V. H. J. de Beer, S. P. A. Louwers, R. Prins, *Catal. Lett.* **1990**, *5*, 273 – 284.
[17] Y. Hamabe, S. Jung, H. Suzuki, N. Koizumi, M. Yamada, *J. Synchrotron Radiat.* **2010**, *17*, 530 – 539.
[18] J. G. Highfield, E. Claude, K. Oguro, *Electrochim. Acta* **1999**, *44*, 2805 – 2814.
[19] P. A. Ferrin, S. Kandoi, J. Zhang, R. Adzic, M. Mavrikakis, *J. Phys. Chem. C* **2009**, *113*, 1411 – 1417.

